Star shape interferometer with reduced vibration sensitivity

J. de la Rosa and E. Gomez

Instituto de Física, Universidad Autónoma de San Luis Potosí,
San Luis Potosí, 78290, México.
e-mail: egomez@ifisica.uaslp.mx

V. M. Valenzuela

Facultad de Ciencias Físico Matemáticas, Universidad Autónoma de Sinaloa,
Sinaloa, 80013, México.

An optical interferometer has a high sensitivity to displacements of the mirrors and other optical elements, something that becomes a source of fluctuations in situations where one is only interested in the phase change due to a sample inserted in one of the paths. A Sagnac interferometer minimizes this sensitivity by having the two beams follow opposite trajectories, so that a mirror displacement gives a similar phase change for both paths, but makes it impossible to insert an element that affects only one path. We present a new kind of interferometer, the Star interferometer, where the two beams still interact with all the optical elements while having different trajectories. We obtain a common phase change in both trajectories by having a different number of turns for each path. Having independent access to both trajectories makes it possible to determine the phase change due to a sample inserted in one of the paths, opening new possibilities for interferometric configurations that maintain a reduced sensitivity to displacements of the optical elements.

1. Introduction

Laser interferometry is used as a tool to measure fundamental constants and test frontier physics [1, 2]. These interferometers opened the way to incredibly sensitive measurements. The best example is the Laser Interferometer Gravitational-Wave Observatory (LIGO) with enough sensitivity to detect gravitational waves [2, 3]. However, most of the interferometric techniques currently used have stability problems as they are susceptible to mechanical and thermal noise [4–8]. One exception is the Sagnac interferometer, because the two counter-propagating beams follow the same path in opposite directions, giving the interferometer good common noise rejection, at the price of the inseparability of their beams. Similar noise rejection is obtained with counter-propagating Mach-Zehnder interferometers [9].

Having different paths allows one to manipulate each beam independently [10–12]. The Mach-Zehnder interferometer using the displaced Sagnac configuration [13] has parallel independent paths while keeping some of the noise rejection properties of the Sagnac interferometer [14]. An interferometer like this is useful to determine the phase change in the light due to the presence of a sample. Any mirror displacement becomes a source of noise for the measurement, making it desirable to work with configurations that are not sensitive to mirror motion.

Here, we present a new type of interferometer that we call "Star" interferometer, which has good common mode noise rejection with beams that follow completely different paths giving rise to a new family of interferometer configurations. The name is related to the star shape of the paths in the in-

terferometer and not to a particular use it may find for astronomy. Both beams interact with the same optical elements giving the interferometer enhanced insensitivity to displacements of these components. We demonstrate experimentally the sensitivity suppression to displacements by scanning simultaneously the Star and a Michelson interferometer. We emphasize that the Star interferometer mantains full sensitivity to phase changes due to samples inserted in one of the paths.

The phase difference between the two interferometric paths depends on the wave vector (k) and the Optical Path Length (OPL). The frequency fluctuations and the vibrations and expansions become a noise source. An equal arms interferometer has no frequency sensitivity. Indeed, the Free Spectral Range (FSR) of a Michelson interferometer is given by [15]

$$\Delta\nu = c/2\Delta L, \tag{1}$$

with ΔL the arm's length difference and c the speed of light. A reduced thermal sensitivity is obtained by mounting the cavity in materials with a small thermal expansion coefficient such as Zerodur [16], ULE materials [16–18] or crystalline silicon [19]. These cavities use clever geometries and mounts to minimize the coupling to the relevant vibration modes [20, 21], and reduce the thermal noise through the use of mirror substrates with high mechanical quality factors [18, 22, 23]. In a Sagnac interferometer a displacement of the mirror changes the OPL of both paths by the same amount. The elimination of the sensitivity to mirror displacements is accompanied by the suppression of frequency sen-
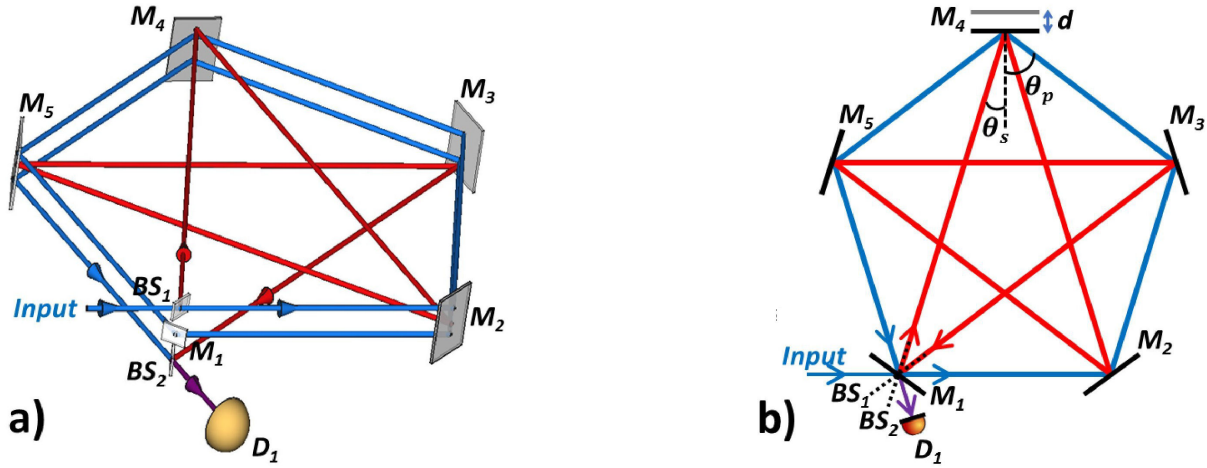
FIGURE 1. a) 3D view of the configuration for the Star interferometer. The laser beam is divided in two paths with the input beam splitter (BS_1). One path makes one complete turn in the star (5b, red) trajectory. The other makes two turns in the pentagon (5a, blue) path. Both beams overlap on the output beam splitter (BS_2) and interfere on the detector (D_1, purple arrow). b) Top view of the interferometer.

sitivity since $\Delta L = 0$ (Eq. (1)). It is possible to recover the frequency sensitivity by introducing an asymmetry between the counter-propagating paths of the Sagnac interferometer [11, 12, 24].

2. Star interferometer principle

Inspired by the Sagnac interferometer, we present here a novel type of interferometer that has reduced vibration sensitivity with a geometry that sends both beams through all the mirrors but not following the same trajectory. We keep the suppression coming from having a common shift of both beams due to the mirror displacement, but now each beam is accessible independently. Figure 1 shows the Star interferometer that has different trajectories for the two beams (pentagon in blue and star in red) and still they share common mirrors. The change in optical phase for each beam in a single turn due to a mirror displacement by d (Fig. 1) is [25]

$$\Delta\phi = 2kd\cos\theta, \qquad (2)$$

with k the magnitude of the wave vector and θ the angle between the beam and the normal to the mirror. The change in the OPL of the two paths in Fig. 1b) is different since the incident angle for the pentagon (θ_p, blue) is not the same as that of the star (θ_s, red). We found that a very close match can be achieved by having m round trips on the pentagon trajectory ($\Delta\phi_p \propto m\cos\theta_p$) and n round trips for the star ($\Delta\phi_s \propto n\cos\theta_s$), that is by making $m\cos\theta_p \simeq n\cos\theta_s$, as we demonstrate below. Figure 1a), for example, shows the case of $m = 2$ round trips for the pentagon and $n = 1$ round trip for the star. The same idea can be extended to other polygons creating a new family of interferometer configurations for each one. They need to be convex symmetric figures in order to achieve simultaneous alignment of both trajectories and must have an odd number of sides so that each trajectory hits all the mirrors, that is, they must be regular polygons with $N = 5, 7, 9, ...$ sides.

3. Vibration sensitivity suppression

Consider a displacement d of one mirror as shown in Fig. 1b). We calculate the phase change in the pentagon and star paths as a function of the number of turns on each one, considering for now that all the figure lies in one plane. The total phase change at the D_1 detector for each path is given by the phase change right at the mirror (Eq. (2)) multiplied by the number of turns. The difference in phase change for two paths, for example, the pentagon (p) with m turns and the star (s) with n turns would be

$$\Delta\phi_p - \Delta\phi_s = 2kd[m\cos(\theta_p) - n\cos(\theta_s)]. \qquad (3)$$

We compare this phase change with that of a Michelson interferometer ($\Delta\phi_M = 2kd$). For a comparison with a Mach-Zehnder (with an incidence angle of $45°$), the phase change is $\sqrt{2}$ times smaller than a Michelson. We define the sensitivity suppression (S) as the ratio of the phase change of the Michelson interferometer compared to that of the Star interferometer, that is

$$S = \frac{\Delta\phi_M}{\Delta\phi_p - \Delta\phi_s} = \frac{1}{m\cos(\theta_p) - n\cos(\theta_s)}. \qquad (4)$$

The closer the denominator is to zero, the bigger the suppression. This is our main result, shown here by this simple calculation, and validated by the experimental demonstration (and by a numerical calculation of the complete OPL). It is a simple but elegant solution, adding multiple turns on an interferometer that has different incident angles on the mirrors in order to obtain a very good suppression to mirror displacements. This result is independent of the size of the interferometer or its operating point. It is important to notice that this works not only for a single mirror of the interferometer, but for all the interferometer as we demonstrate below, so that the complete interferometer has the same vibration sensitivity
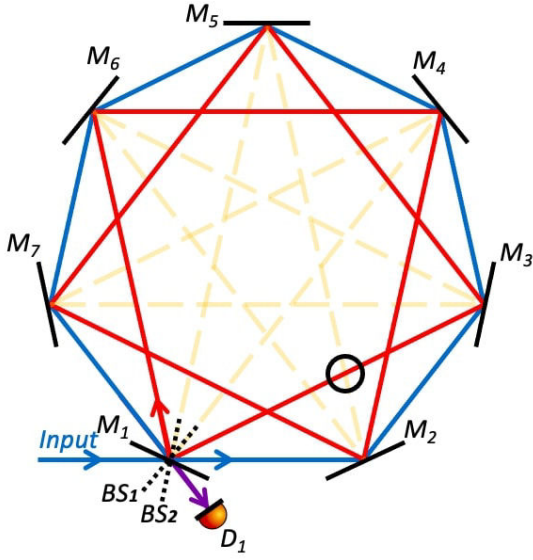
FIGURE 2. Trajectories available in the polygon with $N = 7$ sides, which include the $7a$ in blue, $7b$ in red and $7c$ in yellow. The correct orientation for the input beam and beam splitters (BS_1 and BS_2) depends on the pair of trajectories chosen.

suppression, considering that vibrations correspond to mirror displacements.

Table I gives the phase change rounded to three digits for each of the possible trajectories in polygons with 5, 7 and 9 sides and different number of turns. The result is normalized to the phase change $2kd$ of the Michelson interferometer. In other words, Table I computes the value of $\Phi_m = m \cos \theta$. Each column in Table I is labeled by a number and a letter. The first indicates the number of sides of the polygon. The second determines the trajectory. Starting at the input mirror, a corresponds to the figure obtained when joining each consecutive mirror, as it is the case for the (blue) pentagon of Fig. 1a). b corresponds to the case where we jump by two mirrors as in the (red) star path. The jump in c is by three mirrors, as in the yellow path of Fig. 2, and so on. The angle $\theta_i = \pi[(1/2) - (i/N)]$ is the one used in Eq. (2), with $i = 1, 2, 3, ...$ corresponding to $a, b, c, ...$, and N the number of sides of the polygon.

TABLE I. Normalized phase change for different number of turns ($\Phi_m = m \cos \theta$). Each column indicates the number of sides (N) and trajectory. We highlight with the same color the pair of configurations that give a similar phase change. The numbers have been rounded to three digits.

					Trajectory				
m	$5a$	$5b$	$7a$	$7b$	$7c$	$9a$	$9b$	$9c$	$9d$
1	0.59	0.95	0.43	0.78	0.97	0.34	0.64	0.87	0.98
2	1.18	1.90	0.87	1.56	1.95	0.68	1.29	1.73	1.97
3	1.76	2.85	1.30	2.34	2.92	1.03	1.93	2.60	2.95
4	2.35	3.80	1.74	3.13	3.90	1.37	2.57	3.46	3.94
5	2.94	4.75	2.17	3.91	4.87	1.71	3.21	4.33	4.92

Highlighted pairs of values in the table give configurations with similar phase change and correspond to an interferometer with reduced sensitivity to mirror displacements. For example, the trajectory $5a$ (pentagon (p)) with 5 turns has a very similar phase change to the $5b$ (star (s)) with 3 turns (red in Table I). This would correspond to what is shown in Fig. 1a) but with 5 complete turns of the blue pentagon (instead of 2) and 3 of the star (instead of 1). The difference of the two values ($\Delta \Phi = \Phi_5(p) - \Phi_3(s) = 0.086$) gives the relative phase change at the output of the interferometer, compared to that of a Michelson interferometer, that is, such configuration has a displacement sensitivity (Eq. (4))

$$S = \frac{1}{\Delta \Phi} = 11.7 \qquad (5)$$

times smaller than that of a Michelson. Displacements parallel to the mirror surface have no effect on the interferometer.

Improving the sensitivity suppression relies on making the denominator of Eq. (4) as close to zero as possible, that is, making

$$\frac{m}{n} \simeq \frac{\cos(\theta_s)}{\cos(\theta_p)}, \qquad (6)$$

with θ_p and θ_s the angles corresponding to the trajectories with m and n turns respectively (not limited to the pentagon and star, but to any pair of trajectories on a particular polygon). We need a rational number on the left hand side of Eq. (6) to approximate the number on the right. Incrementally better fractions that achieve this are found by the method of continued fractions. Take for example the case of a polygon with $N = 5$ using the pentagon (a) (blue in Fig. 1a) and star (b) (red) trajectories. The right hand side of Eq. (6) gives $\cos(\pi/10)/\cos(3\pi/10) = (1 + \sqrt{5})/2$, the well known golden ratio. The continued fraction representation is $[1; 1, 1, 1, 1, ...]$ that corresponds to the sequence of fractions

$$\frac{1}{1}, \frac{2}{1}, \frac{3}{2}, \frac{5}{3}, \frac{8}{5}, ..., \qquad (7)$$

that get incrementally closer to the desired value. Each of these fractions (m/n) corresponds to a particular number of turns for the pentagon (m) and the star (n) trajectories. The corresponding suppression (S from Eq. (4)) for each of the above fractions is -2.8, 4.5, -7.2, 11.7, 18.9, ..., whose absolute value indeed grows with consecutive fractions. The fourth fraction (5/3) in the sequence above corresponds to the combination highlighted in Table I with 5 turns of the pentagon ($5a - 5$) and 3 turns of the star ($5b - 3$) (See also Table II).

It is clear that the 4 mirrors ($M_2 - M_5$) in Fig. 1a) have the same suppression (Eq. (5)), and now we analyze what happens with the 3 optical elements (BS_1, M_1, BS_2) that are in the input/output port. We analyze first what happens when each of them is displaced independently for the case of the pentagon with 5 turns and the star with 3 turns. Looking at the mirror M_1, the pentagon path hits that mirror 4 times (instead of 5) and the star path hits it 2 times. A displacement of this element in the direction perpendicular to the mirror

(away from the center) gives a phase change difference (normalized to that of a Michelson) of $\Delta\Phi = 0.449$ and a sensitivity suppression of $S = 2.2$, instead of the $S = 11.7$ calculated for the other mirrors (Eq. (5)). It is clear that a displacement parallel to the mirror surface induces no phase change at all. Similarly, we can calculate what happens with a displacement of the input splitter BS_1. Here, by calculating the full difference in optical paths of the two trajectories due to the splitter displacement, we obtain a normalized phase change difference of $\Delta\Phi = -0.588$ with a displacement perpendicular (south-east direction) to this optical element and no phase change with a displacement parallel to its surface. The same happens with the output splitter BS_2, with $\Delta\Phi = -0.588$ for a perpendicular (north-west) displacement.

The previous discussion shows that we do not obtain a good vibration sensitivity suppression when displacing each of these elements independently, but there is a good suppression when they are fixed with respect to each other and move as a single unit. Assume a displacement of the full unit (BS_1, M_1 and BS_2) perpendicular to the mirror M_1 away from the center. The normalized phase change difference contributions are $\Delta\Phi = 0.449$, $-0.588 \sin(\pi/10)$ and $-0.588 \sin(\pi/10)$ for M_1, BS_1 and BS_2, respectively. Adding them, gives $\Delta\Phi = 0.086$ and a vibration sensitivity suppression of $S = 1/\Delta\Phi = 11.7$, which is exactly the same as any of the other 4 mirrors in the setup. Now, if the displacement of the full unit is parallel to the surface of M_1, then we have $\Delta\Phi = 0$, $-0.588 \cos(\pi/10)$ and $0.588 \cos(\pi/10)$

for M_1, BS_1 and BS_2, respectively, and adding them we get $\Delta\Phi = 0$, that is, perfect suppression for displacements in the parallel direction. The conclusion is that if the three elements BS_1, M_1 and BS_2 move together as a single unit, they have the exact same displacement sensitivity as that of any other mirror. The same result is obtained for any other number of sides of the polygon or trajectories. The complete Star interferometer has therefore the displacement sensitivity suppression (S) that we calculate for the mirror as indicated by Eq. (5).

The suppression value S, for other possible pairs of trajectories is shown in Table II. The third column shows a combination with a suppression ($S = 105.9$) one order of magnitude better than before, achieved by combining the Star $7b$ path (red in Fig. 1b) with 5 turns with the Star $7c$ (yellow) with 4 turns. Combinations that included paths of the $9c$ column of Table I were not included because they do not interact with all the mirrors. The second column shows another combination that has a good suppression ($S = 11.6$) with a small number of turns corresponding to the heptagon $7a$ path (blue in Fig. 3) with 2 turns with the Star $7b$ (red) with 1 turn. This particular combination is the one we demonstrate experimentally (Fig. 4).

For a polygon with $N = 7$ using the trajectories a (blue in Fig. 3) and b (red), the right hand side of Eq. (6) gives $\cos(3\pi/14)/\cos(5\pi/14) \simeq 1.8019$. The continued fraction representation is $[1;1,4,20,...]$ that corresponds to the sequence of fractions

$$\frac{1}{1}, \frac{2}{1}, \frac{9}{5}, \frac{182}{101}, ..., \tag{8}$$

with corresponding suppression $S = -2.9$, 11.6, -237.9, 537.4, ... The second fraction in Eq. (8) corresponds to the one we implement experimentally, with 2 turns on the heptagon ($7a - 2$) and 1 turn in the star b ($7b - 1$) (See Table II). In this case we obtain an order of magnitude improvement with a small number of turns, making the alignment much

TABLE II. Sensitivity suppression S, compared to a Michelson interferometer from the highlighted configurations of Table I, where the path specifies the column and the number of turns from Table I. The value in red is the one we compare against the measurement.

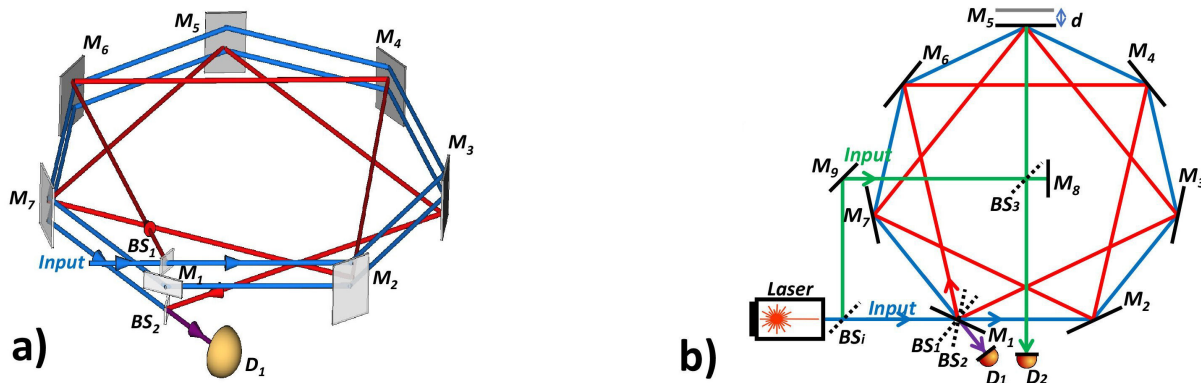| Path 1	$5a-5$	$7a-2$	$7b-5$	$9a-2$	$9a-3$	$9b-3$
Path 2	$5b-3$	$7b-1$	$7c-4$	$9b-1$	$9d-1$	$9d-2$
S	11.7	11.6	105.9	24.2	24.2	24.2

FIGURE 3. a) 3D view of the configuration for the Star interferometer corresponding to two turns of the heptagon $7a - 2$ (blue) with one turn of the Star $7b - 1$ (red). b) Top view of the experimental comparison between the Star and a Michelson interferometer (green). To compare the displacement sensitivity, we move (d) mirror M_5 that is common to both the Michelson and the Star interferometer. We look at the phase change of each interferometer due to exactly the same mirror displacement on detectors D_1 and D_2.
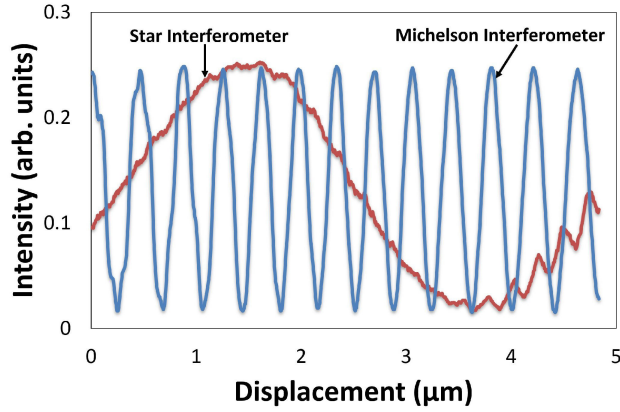
FIGURE 4. Experimental fringes for the Michelson (blue plot, detector D_2 in Fig. 3) and the Star (red plot, detector D_1) interferometers as we displace the common mirror (M_5), when using the configuration $7a - 2$ with $7b - 1$ from Table II (blue and red trajectories in Fig. 3).

simpler. For this particular polygon, another order of magnitude can be obtained by going to 9 turns of the heptagon ($7a-9$) and 5 for the star (b) ($7b-5$). The continued fractions show that further improvement quickly becomes impractical given the number of turns required.

Figure 4 shows the interference fringes obtained simultaneously for the Star (detector D_1) and the Michelson (detector D_2) interferometers, while displacing a common mirror (M_5) with a piezo by 4.8 μm in 168 ms, for the $7a - 2$ and $7b - 1$ (blue and red trajectories in Fig. 3) combination (second column in Table II). The heptagon has a length of 41.9 ± 0.3 cm on each side and the arm's length difference of the Michelson interferometer of $\Delta L = 27.3 \pm 0.4$ cm was chosen to have a similar FSR (Eq. (1)) to that of the Star interferometer (they only differ by $14 \pm 1\%$), so that frequency fluctuations affect both interferometers in the same way. The diode laser has a wavelength of 780 nm (frequency locked to a saturation spectroscopy atomic resonance in the D_2 line of rubidium). Figure 4 shows that for exactly the same displacement of the mirror we obtain a much smaller phase change at the output of the Star interferometer in comparison with that of a Michelson interferometer, similarly to what was done in other reduced sensitivity experimental demonstrations [26]. The measurement clearly demonstrates the reduced sensitivity for mirror displacements, since the same mirror movement gives a phase change of about 12 fringes for the Michelson compared with only one for the Star interferometer. The only thing changing in the measurement is the position of mirror M_5, since the laser frequency is fixed and the frequency response of both interferometers is very similar. The value of the sensitivity suppression is obtained from the ratio of the number of fringes in the Michelson (obtained from a sinusoidal fit) to those of the Star interferometers, for the total displacement shown in Fig. 4. The measured value for the sensitivity suppression is 11.74 ± 0.02, which is consistent with the expected value of 11.6 for this configuration. Sensitivity suppression to a displacement is basically equivalent

to suppression of vibrations or thermal expansions given that the mirror velocity would be much smaller than the speed of light.

As can be seen from the 3D view in Fig. 3a), the setup only requires off the shelf mirrors and beam splitters, carefully measuring their position with a ruler. We use metallic mirrors that maintain a reasonably constant reflectivity at different angles, and input (BS_1) and output (BS_2) economy 30:70 beam splitters (model EBP1). The three elements M_1, BS_1 and BS_2 are mounted in separated mounts in our implementation, to make it easier to align each one independently. In future implementations of the Star interferometer it would be desirable to custom machine a single holder with the correct angles for the three optical components to have it move as a single unit, as discussed before. The alignment procedure takes longer but is not qualitatively different than a typical interferometer, and the particular combination we demonstrate is relatively easy to align. Using polygons with a higher number of sides would affect the robustness of the interferometer due to the increased number of optical components.

The implementation of the Star interferometer requires a small vertical tilt ($\alpha = 0.18 \pm 0.06°$) so that the beam is lowered slightly at each turn (Fig. 3a). The input splitter BS_1 separates the two paths of the interferometer, then a mirror M_1 right below this splitter sends the heptagon path on a second turn and the output splitter BS_2 (EBP1) just below the mirror combines the two paths and sends the light to detector D_1 (Fig. 3). Given that the beams are no longer in a plane, a full 3D calculation is needed. We complemented the analytical results with a numerical calculation of the full OPL.

The vibration sensitivity suppression relies on having $m \cos(\theta_p) \simeq n \cos(\theta_s)$ (Eq. (4)). Adding a vertical tilt (α) of the input beam takes us out of the plane and changes slightly the values of θ_p and θ_s, resulting in a better or worse match of the previous relation, which translates into a different vibration sensitivity suppression. As an example, we show in Fig. 5a) the vibration sensitivity suppression to displacements as a function of the input vertical angle for the configuration that we demonstrate experimentally (Fig. 4), that is, for the configuration $7a - 2$ combined with $7b - 1$. The suppression deteriorates with the input beam vertical angle, but just by very little for small input beam vertical angles. The angle used in the measurement is indicated by the red square that has a suppression very similar to the one at zero vertical input beam tilt. For most of the practical configurations considered in Table II the vertical tilt of the input beam leads to a slightly worse match for the two paths, that is, the suppression of the sensitivity to displacements deteriorates slowly with the tilt angle. The only exception is the configuration of the $9a - 2$ and $9b - 1$ trajectories, where there is a suppression increase limited to 5% at big tilt angles as we show in Fig. 5b).

4. Sensitivity to mirror rotations

To fully characterize the mirror motion, we analyze the effect of a rotation of the mirror M_5 in Fig. 3 along an axis centered
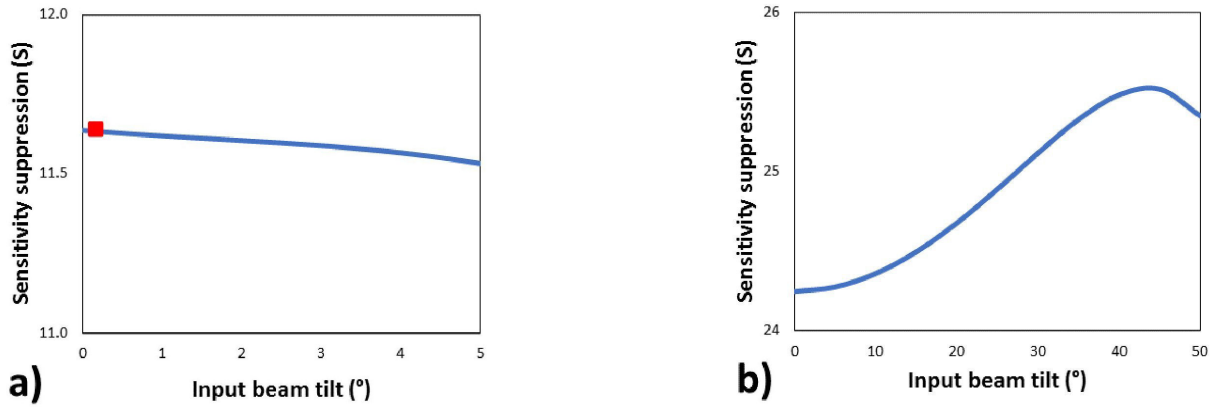
FIGURE 5. a) Displacement sensitivity suppression (S) as a function of the input beam tilt for the combination $7a-2$ with $7b-1$ and b) for the combination $9a-2$ with $9b-1$. The red square in a) corresponds to the tilt angle used in the experimental demonstration.

on the point where the beam hits the mirror, such that the effect is a pure beam rotation, with no displacement. Any displacement introduced by the rotation can be taken into account following the results of the previous section. In the case of a single turn interferometer contained in the plane, the change in phase due to a mirror rotation β is given by $2kD\sin^2\beta \simeq 2kD\beta^2$, where D is the distance from the mirror to the detector, similarly to what is obtained in a Michelson interferometer. The output signal in a Michelson interferometer is more sensitive to mirror displacements than to tilts, and the same happens in the Star interferometer. To show this we consider two contact points from the mirror mount separated by a distance p. Moving both contact points by the same amount d and in the same direction produces a displacement, whereas if the contact point motion is in opposite directions, we get a rotation ($\beta = \arctan(2d/p) \simeq 2d/p$) that introduces a change in phase approximately equal to $8kDd^2/p^2$. For small d, the ratio of phase changes from displacements to that of rotations ($R = p^2/4Dd$) is inversely proportional to d, since one scales linearly and the other quadratically. Taking for example a typical mirror mount with $p = 3.7$ cm and $D = 50$ cm gives a ratio $R = 7 \times 10^2$ for $d = 1$ μm, that is, rotations are much less (700 times) important than displacements. This conclusion remains the same for multiple turns m, since the contribution from rotations scales approximately as $m/2$. Indeed, for $2n$ (or $2n+1$) turns, the change in the output phase is given by $2k[n(\Delta D_a)]\sin^2\beta$ (or $2k[n(\Delta D_a)+\Delta D_b]\sin^2\beta$), with $\Delta D_{a,b}$ the length differences for the two paths for the case of a complete turn (a) and for the distance from the mirror to the detector in the last turn (b). The Star interferometer in the plane has a smaller sensitivity to mirror rotations compared to the Mach-Zehnder interferometer using a displaced Sagnac configuration [13,27].

Figure 6 gives a numerical calculation that shows a comparison of the output phase change as a function of how much we move the contact point (d) for the case of a displacement (blue solid line, both contact points moving in the same direction), and a rotation (red dotted and green dashed line, contact

points moving in opposite direction) for the Star interferometer with the combination $7a-2$ with $7b-1$. We include rotations in the plane and out of the plane of the interferometer. For an interferometer that lies completely in the plane ($\alpha = 0$), both directions of rotations give a contribution similar to the red dotted curve in Fig. 6. At these small tilts, the variations in the overlap of the two paths at the detector due to the beam steering is negligible. The figure confirms that displacements have a much stronger effect than rotations on the output phase and shows the linear and quadratic dependence of each one. The Star configuration suppresses the contributions coming from these displacements independent if they are due to vibrations or expansions.

The tilt angle α has a negligible effect on the displacement sensitivity but produces an increase in the sensitivity to rotations. Figure 7 shows a schematic of the beams hitting one of the mirrors in the interferometer as seen from the side. The figure does not correspond exactly to a particular real configuration, but it is useful to estimate the size of the ef-
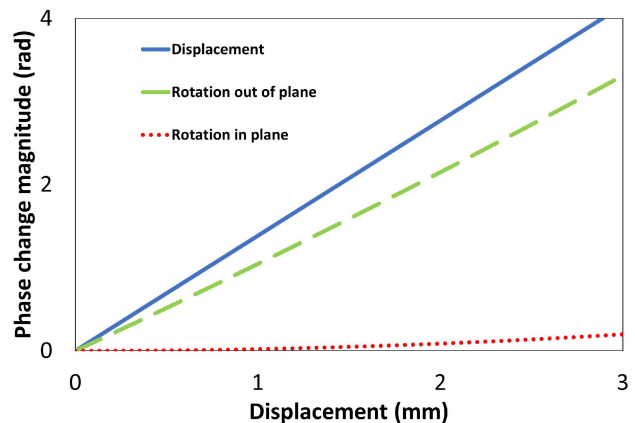

FIGURE 6. Output phase change of the Star interferometer as we move the contact points in the mirror for a pure displacement or rotation, depending if the contact points move in the same or opposite directions. The numerical calculation corresponds to the experimental setup and we include the two possible rotations of the mirror.
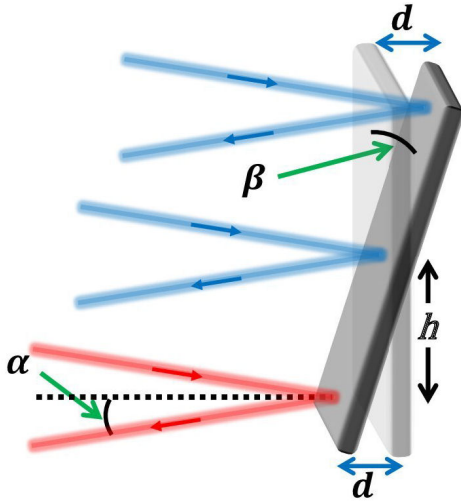
FIGURE 7. Displacement on the different paths introduced by a mirror rotation as seen from the side. The central path hits the rotation pivot and is not displaced, but the paths above and below get displaced by d and $-d$ respectively.

fects of rotations. The blue paths may correspond to the two turns of the path $7a$ and the red to the one turn in path $7b$, as would be the case for example for the second column in Table II. Each trajectory hits the beam at a different heights. Having beams hitting the mirror at different positions is what introduces the sensitivity to rotations in the Mach-Zehnder interferometer using displaced Sagnac configuration [27]. As we rotate the mirror, the central path hits the pivot point and is not displaced, but the paths above and below get displaced

by $d = \pm h \tan \beta$ in this example, where $h = L_1 \sin \alpha$ depends on the tilt α and the round trip distance L_1. The phase change of one path (Eq. (2)) is $2kd\Phi = 2kL_1\Phi \sin \alpha \tan \beta$, where for small rotation angles we have a linear dependence on β and not quadratic as before. The green dashed line in Fig. 6 shows this linear dependence as well as the increase in sensitivity to rotations out of the plane due to the tilt angle. As an example, the configuration with $L_1 = 293.1$ cm as in our experiment, gives a similar sensitivity for displacements and rotations at an input beam tilt of $\alpha = 0.23°$. Residual rotations in our measurements contribute less than 1 % to the signal shown in Fig. 4.

In summary, any mirror motion can be decomposed into displacements and rotations. In this section we show that in the Star interferometer in the plane the displacements have a more important contribution to the phase than those of rotations, but as one moves out of the plane, the relevance of rotations grows. Fortunately, at small tilt angles the contributions from rotations still remain below that of displacements, so that the Star interferometer maintains the immunity to mirror motion of any kind, including expansions coming from temperature variations.

5. Frequency sensitivity

In the previous sections we analyzed the effect of the motion of the optical components in the output signal of the interferometer. In this section we comment on the dependence of the interferometric signal on the laser frequency. The arm's length difference in the two paths of the Star interferometer translates in a Free Spectral Range (FSR) according to Eq. (1) Writing the path length L, of each trajectory in terms of the angle θ of Eq. (2) we have $L = mL_1 = 2Nrm \cos \theta$ with N the number of sides of the polygon and r the radius of the circle enclosing the polygon. The FSR gives $\Delta\nu = (c/2Nr)S$, which is increased by the same suppression factor S. In other words, having reduced displacement sensitivity is connected with wider spectral features.

It may be desirable to have narrow spectral features (with an small FSR) while keeping the insensitivity to mirror motion. Having independent access to the two paths opens the door to novel types of sensors by acting on the phase, polarization or intensity of each path, but brings the usual problems associated with having beams not following the exact same trajectory. One could obtain a narrow frequency response by inserting a transmissive non expanding material in one arm that couples only high frequency vibrational noise [28]. Also one could use the Star interferometer to study the phase change introduced by a sample that is placed in one of the paths of the interferometer. Examples of such measurements can be found in the literature that would benefit immediately from moving to the Star interferometer configuration [10, 29–31]. The sample changes the output signal of the interferometer by changing the phase of only one of the paths, and this measurement will be robust against vibrations or expansions since the mirrors and the rest of the interferometer mantain the demonstrated suppression. Atomic clouds may be placed in beam intersections, like that indicated by a circle in Fig. 2, to implement sensors such as gravimeters or gyroscopes. It would be interesting to extend the ideas presented here for suppressed sensitivity to vibrations in the case of matter wave devices.

6. Conclusion

We present a new interferometer, the Star interferometer, that has reduced sensitivity to vibrations and displacements of the optical elements. The common noise rejection is achieved by having the two paths of the interferometer interact with all the mirrors in the interferometer while following different trajectories. We demonstrate experimentally a particular combination for the Star interferometer that has a sensitivity to displacements 11 times smaller than a Michelson interferometer. There are other combinations available that offer a sensitivity suppression of two orders of magnitude or more. We show that the dominant contribution to the fluctuations come from displacements with a smaller component from rotations. The Free Spectral Range of the interferometer is finite but increases with the same displacement suppression

factor (S). The Star interferometer opens the door to new geometries where one can modify the phase, polarization or intensity of each arm independently while maintaining reduced vibration and displacement sensitivity.

Acknowledgments

1. H. Müller *et al*., Modern Michelson-Morley Experiment using Cryogenic Optical Resonators, *Phys. Rev. Lett.* **91** (2003) 020401, https://doi.org/10.1103/PhysRevLett.91.020401.

2. B. P. Abbott and et al., Observation of Gravitational Waves from a Binary Black Hole Merger, *Phys. Rev. Lett.* **116** (2016) 061102, https://doi.org/10.1103/PhysRevLett.116.061102.

3. B. P. Abbott *et al*., GW151226: Observation of Gravitational Waves from a 22-Solar-Mass Binary Black Hole Coalescence, *Phys. Rev. Lett.* **116** (2016) 241103, https://doi.org/10.1103/PhysRevLett.116.241103.

4. K. Numata, A. Kemery, and J. Camp, Thermal-Noise Limit in the Frequency Stabilization of Lasers with Rigid Cavities, *Phys. Rev. Lett.* **93** (2004) 250602, https://doi.org/10.1103/PhysRevLett.93.250602.

5. L. Chen *et al*., Vibration-induced elastic deformation of Fabry-Perot cavities, *Phys. Rev. A* **74** (2006) 053801, https://doi.org/10.1103/PhysRevA.74.053801.

6. T. Nazarova, F. Riehle, and U. Sterr, Vibration-insensitive reference cavity for an ultra-narrow-linewidth laser, *Appl. Phys. B* **83** (2006) 531, https://doi.org/10.1007/s00340-006-2225-y.

7. S. A. Webster, M. Oxborrow, and P. Gill, Vibration insensitive optical cavity, *Phys. Rev. A* **75** (2007) 011801(R), https://doi.org/10.1103/PhysRevA.75.011801.

8. A. D. Ludlow *et al*., Compact, thermal-noise-limited optical cavity for diode laser stabilization at 1×10^{-15}, *Opt. Lett.* **32** (2007) 641, https://doi.org/10.1364/OL.32.000641.

9. Y. Chen *et al*., Interferometers for Displacement-Noise-Free Gravitational-Wave Detection, *Phys. Rev. Lett.* **97** (2006) 151103, https://doi.org/10.1103/PhysRevLett.97.151103.

10. M. Xiao, et al., Measurement of Dispersive Properties of Electromagnetically Induced Transparency in Rubidium Atoms, *Phys. Rev. Lett.* **74** (1995) 666, https://doi.org/10.1103/PhysRevLett.74.666.

11. G. T. Purves, C. S. Adams, and I. G. Hughes, Sagnac interferometry in a slow-light medium, *Phys. Rev. A* **74** (2006) 023805, https://doi.org/10.1103/PhysRevA.74.023805.

12. G. Jundt *et al*., Non-linear Sagnac interferometry for pump-probe dispersion spectroscopy, *Eur. Phys. J. D* **27** (2003) 273.

13. T. Nagata *et al*., Beating the Standard Quantum Limit with Four-Entangled Photons, *Science* **316** (2007) 726, https://doi.org/10.1126/science.1138007.

14. M. Mičuda *et al*., Highly stable polarization independent Mach-Zehnder interferometer, *Rev. Sci. Instrum*. **85** (2014) 083103, https://doi.org/10.1063/1.4891702.

15. B. E. A. Saleh and M. C. Teich, Fundamentals of Photonics (John Wiley & Sons, Ltd, New York, 1991), pp. 246-256, https://doi.org/10.1002/0471213748.ch1.

16. J. Alnis *et al*., Subhertz linewidth diode lasers by stabilization to vibrationally and thermally compensated ultralow-expansion glass Fabry-Pérot cavities, *Phys. Rev. A* **77** (2008) 053809, https://doi.org/10.1103/PhysRevA.77.053809.

17. T. Legero, T. Kessler, and U. Sterr, Tuning the thermal expansion properties of optical reference cavities with fused silica mirrors, *J. Opt. Soc. Am. B* **27** (2010) 914, https://doi.org/10.1364/JOSAB.27.000914.

18. Y. Y. Jiang *et al*., Making optical atomic clocks more stable with 10-16 level laser stabilization, *Nat. Photonics* **5** (2011) 158.

19. T. Kessler *et al*., A sub-40-mHz-linewidth laser based on a silicon single-crystal optical cavity, *Nat. Photonics* **6** (2012) 687.

20. B. C. Young *et al*., Visible Lasers with Subhertz Linewidths, *Phys. Rev. Lett.* **82** (1999) 3799, https://doi.org/10.1103/PhysRevLett.82.3799.

21. S. Amairi *et al*., Reducing the effect of thermal noise in optical cavities, *Appl. Phys. B* **113** (2013) 233.

22. M. Notcutt, et al., Contribution of thermal noise to frequency stability of rigid optical cavity via Hertz-linewidth lasers, *Phys. Rev. A* **73** (2006) 031804(R), https://doi.org/10.1103/PhysRevA.73.031804.

23. J. Millo *et al*., Ultrastable lasers based on vibration insensitive cavities, *Phys. Rev. A* **79** (2009) 053829, https://doi.org/10.1103/PhysRevA.79.053829.

24. L. Del Bino, *et al.*, Symmetry Breaking of Counter-Propagating Light in a Nonlinear Resonator, *Sci. Rep.* **7** (2017) 43142, https://doi.org/10.1038/srep43142.

25. F. Pedrotti, L. Pedrotti, and L. Pedrotti, *Introduction to optics* (Prentice Hall, 2006).

26. J. A. Ferrari and E. M. Frins, Single-element interferometer, *Optics communications* **279** (2007) 235.

27. J. Martínez-Rincón *et al.*, Ultrasensitive inverse weak-value tilt meter, *Opt. Lett.* **42** (2017) 2479, https://doi.org/10.1364/OL.42.002479.

28. N. Arias *et al*., Low phase noise beams for Raman transitions with a phase modulator and a highly birefringent crystal, *Opt. Express* **25** (2017) 5290.

29. J. Jin *et al*., Thickness and refractive index measurement of a silicon wafer based on an optical comb, *Opt. Express* **18** (2010) 18339.

30. R. Bommareddi, Applications of Optical Interferometer Techniques for Precision Measurements of Changes in Tempera-ture, Growth and Refractive Index of Materials, *Technologies* **2** (2014) 54.

31. A. Börzsönyi *et al*., Advances and limitations of phase dispersion measurement by spectrally and spatially resolved interferometry, *Opt. Commun.* **281** (2008) 3051.